Journal of Materials Chemistry A

PAPER

View Article Online
View Journal

Cite this: DOI: 10.1039/c8ta04218g

A biomimetic *Setaria viridis*-inspired electrode with polyaniline nanowire arrays aligned on MoO_3@polypyrrole core–shell nanobelts†

Ying Liu,[a] Le Li,[a] Jixin Zhu,[b] Jingsan Xu,[c] Siliang Liu,[a] Yufeng Wang,[a] Chao Zhang *[a] and Tianxi Liu *[a]

Inspired by multi-scale structures mimicking *Setaria viridis*, herein, arrays of vertically aligned polyaniline (PANI) nanowires on MoO_3/polypyrrole (PPy) core–shell nanobelts have been successfully synthesized *via* a two-step wet-chemistry strategy, including a simple *in situ* oxidative polymerization of pyrrole on MoO_3 nanobelts, followed by an *in situ* oxidative polymerization of aniline on the MoO_3/PPy core–shell nanobelts. By mimicking the hierarchically multi-scale topography of *Setaria viridis* for tailoring the nanostructures and functions of the electrode materials, in the resultant MoO_3/PPy/PANI composites, the MoO_3 nanobelt core acts as the "stalk" surrounded by conducting polymers, whereas the intermediate PPy functions as the buffer "grain" connecting the MoO_3 and PANI nanowires, which provides good structural stability as well as an efficient electron transfer pathway. Moreover, the outermost PANI nanowire arrays act as the "bristles" allowing fast transport of ions and electrons between the electrodes. Due to their compositional and structural superiority, the as-obtained MoO_3/PPy/PANI composites deliver excellent electrochemical energy storage performance including a high specific capacitance of 1315 F g^{-1} at 0.5 A g^{-1}, a high energy density of 63 W h kg^{-1} and an excellent cycling stability (capacitance retention of 86% at 10 A g^{-1} after 20 000 cycles). The easy synthesis and excellent electrode performance of the MoO_3/PPy/PANI composites make them attractive candidates as promising electrode materials for high-performance supercapacitors.

Received 7th May 2018
Accepted 18th June 2018

DOI: 10.1039/c8ta04218g

rsc.li/materials-a

Introduction

Supercapacitors, one of the most promising electrochemical energy storage systems, have attracted enormous attention in various applications in electric vehicles, portable electronics, *etc.*[1,2] Compared with batteries, supercapacitors possess tremendously superior properties such as high power density, long cycle lifetime, low cost and easy operation.[3] Generally, supercapacitors can be classified into two categories according to their diverse energy storage mechanisms, namely, electric double layer capacitors (EDLCs) and pseudocapacitors.[4] EDLCs typically store energy by reversible adsorption/desorption of ions on the surface of electrode materials like high-surface-area carbon materials such as graphene,[5] carbon nanotubes,[6] and carbon black.[7] In contrast, pseudocapacitors store energy by electron charge transfer derived from the faradaic reactions of conducting polymers[6,8,9] and transition metal oxides.[10–13] Pseudocapacitors basically have larger capacitance values compared with those of EDLCs owing to their ability to store energy in the bulk phases of electrodes.[14] However, the irreversible agglomeration of pseudocapacitive materials upon cycling would lead to a dramatic degradation of capacitances.[14] Besides, the unsatisfactory electrical conductivity of pseudocapacitive materials inevitably leads to slow faradaic redox kinetics, which

[a]State Key Laboratory for Modification of Chemical Fibers and Polymer Materials, College of Materials Science and Engineering, Innovation Center for Textile Science and Technology, Donghua University, Shanghai 201620, P. R. China. E-mail: czhang@dhu.edu.cn; txliu@fudan.edu.cn; txliu@dhu.edu.cn

[b]Shaanxi Institute of Flexible Electronics (SIFE), Northwestern Polytechnical University (NPU), 127 West Youyi Road, Xi'an 710072, China

[c]School of Chemistry, Physics and Mechanical Engineering, Queensland University of Technology, Brisbane, QLD 4001, Australia

† Electronic supplementary information (ESI) available: SEM images of MoO_3 after grinding, MoO_3/PPy-1, MoO_3/PPy-3, PPy, and PANI. Schematic illustration of the formation of MoO_3/PANI/PPy. SEM images of MoO_3/PANI-1, MoO_3/PANI-2 and MoO_3/PANI-3. TEM images of MoO_3/PANI-2 and MoO_3/PANI/PPy. SEM images of MoO_3/PANI/PPy. CV curves of MoO_3/PPy-1, MoO_3/PPy-2 and MoO_3/PPy-3. Specific capacitances of MoO_3/PPy-1, MoO_3/PPy-2 and MoO_3/PPy-3. CV curves of MoO_3/PANI-1, MoO_3/PANI-2 and MoO_3/PANI-3. Specific capacitances of MoO_3/PANI-1, MoO_3/PANI-2 and MoO_3/PANI-3. CV curves of MoO_3/PANI/PPy at various scan rates. TGA curves of MoO_3, MoO_3/PANI and MoO_3/PPy/PANI. Specific capacitances of MoO_3/PANI/PPy at various current densities. Self-discharge curve of the supercapacitor device after charging at 1 V for 15 min. Cycling stabilities of the MoO_3, MoO_3/PPy, MoO_3/PPy/PANI, MoO_3/PANI, PPy and PANI electrodes for 3000 charge/discharge cycles at 2 A g^{-1}. Cycling stability of the MoO_3/PPy/PANI electrodes for 20 000 charge/discharge cycles at a current density of 10 A g^{-1}. See DOI: 10.1039/c8ta04218g

would dramatically hinder the practical application of pseudocapacitive materials.[15,16]

To solve these problems, many efforts have been made to improve the electrochemical performance of pseudocapacitive materials by rationally designing hierarchically nanostructured composite materials, simultaneously enhancing ion/electron transport.[17,18] In particular, the design of electrode materials with a nanowire array structure is attractive for achieving high performance in terms of electrochemical energy storage due to their large surface area, short diffusion paths for ions and electrons and excellent structural stability upon cycling.[19] In addition, the construction of composite electrode materials tends to create fascinating electrodes combining the advantages of each component with a unique synergistic effect. Therefore, the composition of various pseudocapacitive materials associated with outstanding electrode performance has been extensively investigated.[20,21] However, it still remains challenging to exploit composition rules for the design and synthesis of composite electrodes made up of conducting polymers and transition metal oxides to achieve an outstanding electrochemical performance.

The abundance of natural structures with well-known stability, geometry configuration, surface wettability and mechanical properties provides endless inspiration and clues for the rational design of nanostructured active materials with the desired performance.[22,23] *Setaria viridis* is a plant commonly found around the world, and it has extremely high structural stability especially under harsh wind conditions. Specifically, a biomimetic *Setaria viridis*-inspired imprinted adsorbent to remove drug contaminants from wastewater was prepared using a two-step surface-initiated atom transfer radical polymerization in a green alcohol/water solvent mixture.[24] However, the morphology of this adsorbent is not as perfect as that of *Setaria viridis*. Still, this adsorbent showed good thermal and chemical stability as well as enhanced adsorption selectivity and kinetics for environmental applications. In the spikelet structure of *Setaria viridis*, the inner stalk functions as the supporting material surrounded by vertically aligned thin bristles, and the small intermediate grains connect the stalk and the bristles together. Learning from the delicate multi-scale structures of *Setaria viridis*, we propose the construction of biomimetic electrode architectures employing a two-step *in situ* oxidative polymerization inspired by *Setaria viridis*. The *Setaria viridis*-like structure is advantageous for use as a high-performance electrode material for supercapacitors. First, the inner "stalk" not only provides large ion reservoirs but also homogeneously immobilizes the conducting polymer shells. Second, the intermediate "grain" could effectively connect the inner and the outer part to improve the structural stability of the whole electrode material. Third, the outermost "bristles" allow fast adsorption/desorption of H^+ ions in the frameworks and rapid transportation of electrons. Herein, as a proof-of-concept, a MoO_3 nanobelt is chosen to function as the stalk, and vertically aligned polyaniline (PANI) nanowire arrays are chosen to function as the outermost thin bristles. Furthermore, an ultrathin polypyrrole (PPy) shell is used to bridge the MoO_3 nanobelts and PANI nanowire arrays, and is chosen to function as the intermediate grains. In the ternary composites, the MoO_3 core consists of a bilayer network of edge-sharing MoO_6 octahedra. The bilayers are stacked and bonded to adjacent layers by van der Waals forces, which make the structures suitable for the insertion of ions such as H^+ ions, and its multiple oxidation states can readily enable rich redox reactions for energy storage.[25–27] The small intermediate grains of PPy can function as the buffer and connection layer between the MoO_3 stalk and the PANI bristles, which could improve the conductivity throughout the electrodes and thus improve the electron transfer. The outermost PANI bristles have a large surface area due to their nanowire array morphology, which is ideal for preventing their agglomeration upon cycling as well as allowing fast transport of H^+ ions and electrons.

Experimental

Materials

Sodium molybdate dihydrate ($Na_2MoO_4 \cdot 2H_2O$, AR), sodium chloride (NaCl, AR), hydrochloric acid (HCl, 37%), ethanol (AR grade), concentrated sulfuric acid (H_2SO_4 96.5–98%) and ammonium persulfate (APS, AR) were purchased from Sinopharm Chemical Reagent Co. Ltd. Pyrrole and aniline monomers (AR grade) were obtained from Sigma-Aldrich and distilled before use. Deionized water (DI water) was used throughout the experiments. All these chemicals were used as received without further purification unless specified.

Preparation of MoO_3 nanobelts

The MoO_3 nanobelts were synthesized using a literature method.[28] In a typical procedure, $Na_2MoO_4 \cdot 2H_2O$ (1.21 g) and NaCl (0.6 g) were fully dissolved in 60 mL of DI water with vigorous stirring. The pH of the solution was adjusted to 1.0 with 3 M HCl. The solution was transferred into a 100 mL Teflon-lined stainless-steel autoclave and heated at 180 °C for 24 h. The powder products were collected by filtration, washed with DI water, and then dried at 60 °C under vacuum.

Preparation of MoO_3/PPy composites

MoO_3/PPy with a core–shell structure was prepared by *in situ* oxidative polymerization of pyrrole on the MoO_3 template using APS as an oxidizing agent. 20 mg of MoO_3 nanobelts were dispersed in 80 mL of DI water by vigorous stirring and then the desired amounts of pyrrole were added and the resulting mixture stirred at 0 ± 2 °C. Control of the reaction temperature was achieved by using a cryogenic coolant circulating pump (DLSB-5/20). 20 mL of the APS solution was then added dropwise, and the mole ratio of APS to aniline was 1/2. After reacting for 12 h at 0 ± 2 °C, the precipitates were filtered, washed with DI water and dried under vacuum at 60 °C for 12 h. A series of samples prepared with different initial amounts of pyrrole (*i.e.*, 100, 200 and 400 μL) were labelled as MoO_3/PPy-1, MoO_3/PPy-2, and MoO_3/PPy-3, respectively. For comparison, neat PPy was also prepared through the above-mentioned process in the absence of MoO_3.

Preparation of MoO_3/PANI composites

The MoO_3/PANI binary composites were prepared by *in situ* oxidative polymerization of aniline on the MoO_3 template using APS as an oxidizing agent. Firstly, the desired amounts of MoO_3 nanobelts were suspended in 60 mL of 0.5 M H_2SO_4 solution. 5 mmol of aniline was added, and the suspension was stirred at 0 ± 2 °C. 40 mL of 0.5 M H_2SO_4 solution containing APS was added dropwise with an APS/aniline mole ratio of 1/2 and the reaction was kept stirring for another 12 h at 0 ± 2 °C. Finally, the precipitates were filtered, washed with DI water, and then dried under vacuum at 60 °C for 12 h. A series of samples prepared with different initial amounts of MoO_3 (*i.e.*, 50, 100 and 200 mg) were labelled as MoO_3/PANI-1, MoO_3/PANI-2, and MoO_3/PANI-3, respectively. For comparison, neat PANI was also prepared through the above-mentioned process in the absence of MoO_3.

Preparation of MoO_3/PPy/PANI and MoO_3/PANI/PPy composites

The MoO_3/PPy/PANI ternary composites were synthesized by an *in situ* chemical oxidative polymerization of aniline using the as-prepared MoO_3/PPy-2 as a template, while the MoO_3/PANI/PPy composites were synthesized by an *in situ* chemical oxidative polymerization of pyrrole using the as-prepared MoO_3/PANI-2 as a template. The processes were similar to those used for the preparation of MoO_3/PANI and MoO_3/PPy binary composites. Typically, for the synthesis of MoO_3/PPy/PANI, MoO_3/PPy (100 mg) was suspended in 80 mL of 0.5 M H_2SO_4 solution. 5 mmol of aniline was added, and the suspension was stirred at 0 ± 2 °C. 20 mL of 0.5 M H_2SO_4 solution containing APS was added dropwise with an APS/aniline mole ratio of 1/2, and the reaction was kept stirring for 12 h at 0 ± 2 °C. Finally, the precipitates denoted as MoO_3/PPy/PANI were filtered, washed with DI water, and then dried under vacuum at 60 °C for 12 h. For the synthesis of MoO_3/PANI/PPy, 20 mg of MoO_3/PANI was dispersed in 80 mL of DI water by vigorous stirring and then the desired amounts of pyrrole were added and the resulting mixture stirred at 0 ± 2 °C. 20 mL of the APS solution was added dropwise, and the mole ratio of APS to aniline was 1/2. After stirring for 12 h at 0 ± 2 °C, the precipitates denoted as MoO_3/PANI/PPy were filtered, washed with DI water, and then dried under vacuum at 60 °C for 12 h.

Characterization

The morphologies of the as-synthesized products were studied by field-emission scanning electron microscopy (FESEM, JEOL JSM-7001F) and transmission electron microscopy (TEM, JEOL JEM-2100). The SEM images of the samples after cycling were obtained by washing the electrodes with NMP, ethanol and water several times and then collecting the powder by filtration. The crystalline phases of the obtained products were characterized by X-ray diffraction on a Bruker D8 Advance. The Raman spectra were recorded on a DXR spectrometer using a 532 nm laser line.

Electrochemical measurements

The working electrode was fabricated as follows: a homogeneous slurry was fabricated by mixing active materials, acetylene black and PVDF (Kynar HSV900, Arkema) in a mass ratio of 8 : 1 : 1, and then the slurry was coated onto a graphite paper current collector (1×1 cm^2) followed by drying at 80 °C overnight. A 0.5 M H_2SO_4 aqueous solution was used as an electrolyte. For three-electrode measurements, platinum wire and a saturated calomel electrode (SCE) were used as the counter and reference electrodes, respectively. For two-electrode measurements, the pieces of graphite paper loaded with electrode materials were separated with a cellulose separator and assembled. Electrochemical impedance spectroscopy (EIS) was performed in the frequency range from 10^6 to 10^{-2} Hz with an AC voltage amplitude of 5 mV. The electrochemical performance was evaluated by cyclic voltammetry (CV) and galvanostatic charge–discharge experiments. Eqn (1) was used to calculate the specific capacitances of active materials from the galvanostatic charge/discharge curves in a three-electrode configuration:

$$C_{sp} = \frac{It}{mV} \quad (1)$$

where I is the discharge current, m is the mass of active materials, t is the discharge time, and V is the working voltage range.

The energy density (E) and power density (P) based on a symmetric two-electrode supercapacitor were calculated using the following equations:

$$C = \frac{It}{mV} \quad (2)$$

$$E = \frac{1}{2}C \times \frac{1}{3.6}V^2 \quad (3)$$

$$P = \frac{3600E}{t} \quad (4)$$

where C is the capacitance of the symmetric two-electrode supercapacitor device, I is the discharge current, t is the discharge time, m is the total mass of the two electrodes and V is the operation potential window. The mass loading of the electrodes was controlled at ~1.5 mg cm^{-2}, and two electrodes with similar active material loadings were assembled into the supercapacitor devices.

Results and discussion

Fig. 1a illustrates the synthetic route for the MoO_3/PPy/PANI composites consisting of two steps. First, the MoO_3 nanobelts as the growth template guided the adsorption and subsequent *in situ* oxidative polymerization of pyrrole using ammonium persulphate (APS) as an initiator, thus obtaining the MoO_3/PPy core–shell composites. Second, the MoO_3/PPy composites were chosen as the growth template leading to a vertical alignment of PANI nanowires on their surfaces, thus forming the ternary composites denoted as MoO_3/PPy/PANI. By mimicking the structure of *Setaria viridis* (Fig. 1b), in the MoO_3/PPy/PANI

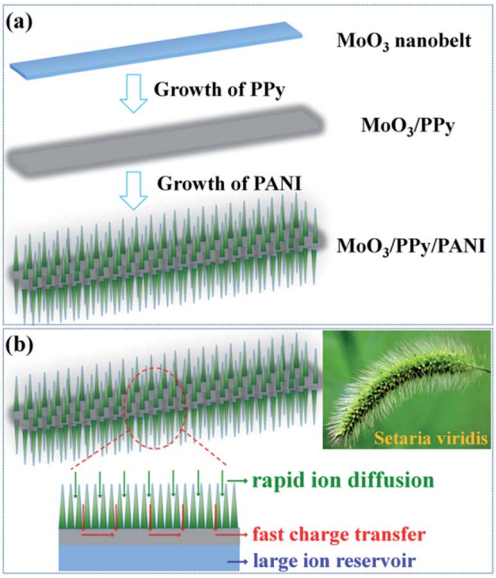

Fig. 1 (a) Schematic illustration of the preparation of the MoO_3/PPy/PANI. (b) Illustration of the MoO_3/PPy/PANI electrodes inspired by a biomimetic *Setaria viridis*-like structure with efficient charge and ion transfer within the electrodes.

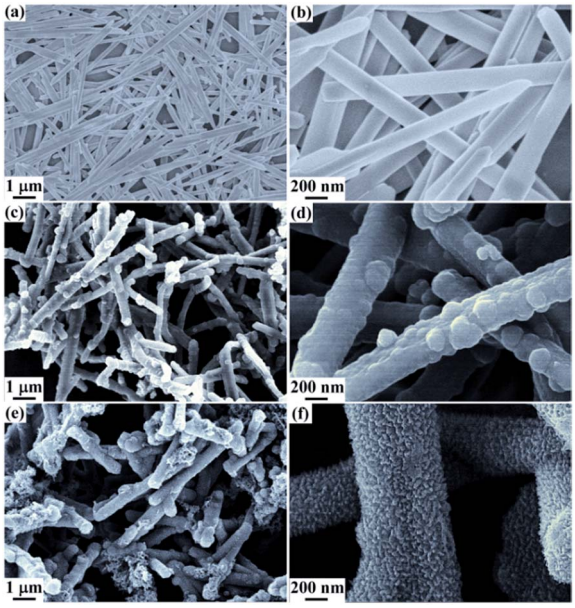

Fig. 2 SEM images of (a and b) MoO_3, (c and d) MoO_3/PPy and (e and f) MoO_3/PPy/PANI at low and high magnification, respectively.

ternary composites, the MoO_3 nanobelt core acts as a large ionic reservoir due to its two-dimensional (2D) layered structure, while the intermediate PPy layer accommodates the volume expansion of embedded MoO_3 as well as promoting charge transfer for the ternary composites. In addition, the outermost PANI nanowire arrays allow fast adsorption/desorption of H^+ ions in the frameworks and rapid transportation of electrons. Therefore, due to the structural features with largely improved ion and electron transfer, the resultant MoO_3/PPy/PANI composites exhibit high electrical integrity and structural stability as a promising electrode material for supercapacitors.

Scanning electron microscopy (SEM) and transmission electron microscopy (TEM) characterizations were carried out to investigate the morphological evolution from MoO_3 to MoO_3/PPy/PANI. The MoO_3 templates illustrate a belt morphology with a width of 150–300 nm, a length of 3–8 μm and a thickness of 25–40 nm (Fig. 2a and b and S1a and b†). The TEM images of MoO_3 further reveal that the nanobelts have smooth surfaces (Fig. 3a and b). MoO_3 nanobelts were successfully coated with ultrathin PPy layers by *in situ* polymerization of pyrrole. The thicknesses of the surrounding PPy layers on the MoO_3 nanobelts were easily controlled by adding various amounts of pyrrole (100, 200 and 400 μL) while keeping all other parameters constant. The resultant MoO_3/PPy composites were denoted as MoO_3/PPy-1, MoO_3/PPy-2 and MoO_3/PPy-3 with increasing feeding content of PPy. Fig. 2c and d show the representative SEM images of the as-synthesized MoO_3/PPy-2 composites, while Fig. S2a and b (ESI†) show the SEM images of MoO_3/PPy-1 and MoO_3/PPy-3, respectively. All the MoO_3/PPy composites exhibit a nanobelt morphology, and an apparent aggregation of PPy particles could be observed in the MoO_3/PPy-3 composites (Fig. S2b, ESI†). The TEM images of MoO_3/PPy-2 (Fig. 3c and d) clearly show that the edges of the MoO_3 nanobelts have obviously become blunt due to uniform PPy coatings, and the PPy shell with a thickness of ~80 nm is wrapped on the outer surface of the MoO_3 nanobelts. The uniform PPy layers facilitate the subsequent growth of PANI nanowire arrays on the surface of the MoO_3/PPy due to the presence of pyrrolic groups for the adsorption and *in situ* growth of PANI. The TEM images of MoO_3/PPy/PANI (Fig. 3e and f) indicate that vertically aligned PANI nanowire arrays are uniformly attached on both sides of the MoO_3/PPy. The SEM images of MoO_3/PPy/PANI (Fig. 2e and f) also indicate that PANI nanowires have uniform nanowire

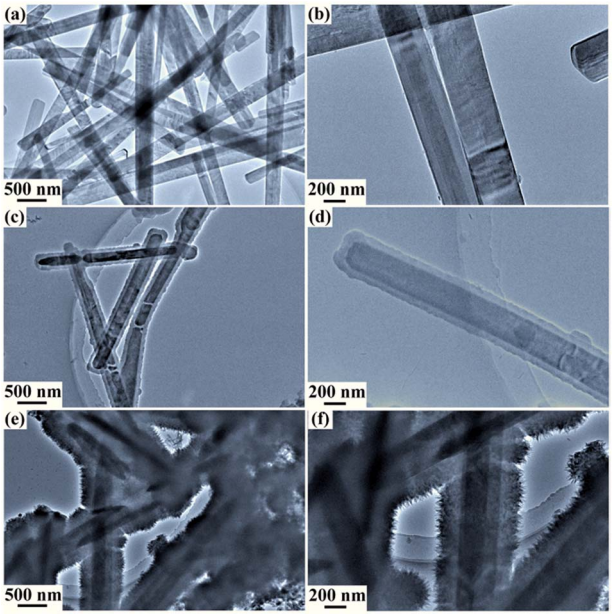

Fig. 3 TEM images of (a and b) MoO_3, (c and d) MoO_3/PPy and (e and f) MoO_3/PPy/PANI at low and high magnification, respectively.

structures of ~100 nm length, reflecting that MoO_3/PPy composites are ideal templates for the growth of PANI nanowire arrays. For comparison, the SEM images of neat PPy (Fig. S3, ESI†) and PANI (Fig. S4, ESI†) exhibit the morphologies of the nanospheres and nanofibers, respectively.

Reference samples were also prepared to investigate the effects of different combination orders of MoO_3, PPy and PANI. Therefore, ternary composites were fabricated by reversing the polymerization sequence of PPy and PANI, as illustrated in Fig. S5 (ESI†). Direct growth of PANI on the MoO_3 nanobelts was achieved, and a homogeneous immobilization of PANI nanowire arrays on the MoO_3 nanobelts was observed, and the resultant composites were denoted as MoO_3/PANI-1, MoO_3/PANI-2 and MoO_3/PANI-3 with increasing feeding content of PANI. The SEM images of the MoO_3/PANI composites (Fig. S6, ESI†) indicate that the PANI nanowires become more and more densely stacked with increasing content of PANI. In addition, the lengths of the PANI nanowire arrays within the MoO_3/PANI composites are ~500 nm (Fig. S7a and b, ESI†), slightly larger than those within the MoO_3/PPy/PANI composites (~400 nm). The MoO_3/PANI/PPy composites were then prepared by using MoO_3/PANI-2 and pyrrole as the template and monomer, respectively. The SEM and TEM images of the MoO_3/PANI/PPy (Fig. S7c and d and S8, ESI†) indicate that the polymerization of pyrrole monomers takes place on the surface of MoO_3/PANI composites rather than in the bulk. The outermost shells of the MoO_3/PANI/PPy are densely polymeric coatings instead of nanowires (Fig. S8a and 8b, ESI†), indicating that the MoO_3/PANI structures are entirely surrounded by the PPy coating. Unless otherwise specified, in the following text, MoO_3/PPy and MoO_3/PANI refer to the MoO_3/PPy-2 and MoO_3/PANI-2 samples, respectively.

X-ray diffraction (XRD) measurements were conducted to monitor the crystal structures of the resultant samples. Neat MoO_3 (Fig. 4a) shows sharp diffraction patterns which can be indexed to the α-MoO_3 phase of the hexagonal crystals (JCPDS no. 05-0508).[29] The MoO_3/PANI, MoO_3/PPy, and MoO_3/PPy/PANI samples show a series of diffraction patterns ascribed to the α-MoO_3 crystals, indicating that no crystalline changes occur for the MoO_3 upon the *in situ* polymerization of PPy and PANI. For neat PPy, a broad diffraction pattern is observed at $2\theta = \sim 25°$, which is derived from the scattering of amorphous PPy.[30] The PANI sample exhibits two broad peaks at $2\theta = 21°$ and 26°, which correspond to the periodicity parallel and perpendicular to PANI chains, respectively.[31,32] For the MoO_3/PPy/PANI sample, the diffraction patterns validate the successful composition of MoO_3, PPy and PANI. The interactions between MoO_3 and these conducting polymers were investigated with Raman spectroscopy (Fig. 4b). The sharp Raman peaks of the MoO_3, which are centered at 242, 290, 338, 380, 660, 818, and 998 cm^{-1}, respectively, indicate the high purity of α-MoO_3 crystals.[29,33] For neat PPy, there are two broad bands at 1361 and 1560 cm^{-1}, respectively, corresponding to the C=C backbone stretching and the ring-stretching mode, respectively.[34] For neat PANI, there exist several characteristic peaks revealing the structures of proton-doped PANI, such as peaks of the out-of-plane amine ring deformations at 412 cm^{-1}, the C–H out-of-plane ring deformation vibration at 583 cm^{-1}, the bending of the quinoid ring at 1165 cm^{-1}, the C–H bending of the benzenoid ring at 1236 cm^{-1}, the C=C stretching of the benzenoid ring at 1470 cm^{-1}, the C=C stretching of the quinoid ring at 1587 cm^{-1}, and the aromatic C–H out of-plane bending at 810 cm^{-1}.[35] Besides, the characteristic peak of PPy (for neat PPy) at 1560 cm^{-1} shifts to 1588 cm^{-1} in the Raman spectra of both MoO_3/PPy and MoO_3/PPy/PANI samples, which is attributed to interactions such as the strong coordination bonding between PPy and MoO_3. A similar blue shift of Raman peaks in the MoO_3/PPy/PANI sample compared with neat PANI confirms that other strong interactions such as π–π interactions also exist between the PPy layer and the PANI nanowires.

The cyclic voltammetry (CV) curves of the MoO_3/PPy electrodes in the acidic electrolyte are showed in Fig. S9a (ESI†). The shapes of the CV curves are distorted with mirror-image symmetry, and a couple of oxidation/reduction peaks are observed, indicating that faradaic capacitances exist in the MoO_3/PPy electrodes. The MoO_3/PPy-2 electrode shows relatively larger specific capacitances than those of the MoO_3/PPy-1 and MoO_3/PPy-3 electrodes at the same discharge current density (Fig. S9b, ESI†). A higher charge storage ability is found in the MoO_3/PPy-2 sample, indicating that an appropriate thickness of the PPy layer is crucial for boosting the electrochemical properties of the MoO_3/PPy composites due to the balance between the diffusion path length and the electrical conductivity derived from the ultrathin PPy layers. Moreover, well-defined redox peaks corresponding to the doping and dedoping of protons in the PANI chains during the charge/discharge processes were observed in the CV curves of the MoO_3/PANI electrodes (Fig. S10a, ESI†), suggesting that they have pseudocapacitive characteristics. The current density in the MoO_3/PANI-2 electrode was larger than those of the MoO_3/PANI-1 and MoO_3/PANI-3 electrodes, revealing the higher specific capacitance of the MoO_3/PANI-2 electrode (Fig. S10b, ESI†). The uniformly distributed PANI nanowire arrays on the MoO_3 nanobelts not only improve the electrochemical utilization of PANI but also shorten the diffusion path length for both ions and electrons.

Fig. 5a illustrates the CV curves of the MoO_3/PPy/PANI composites and their single components and binary MoO_3/PANI and MoO_3/PPy composites at a scan rate of 10 mV s^{-1}. From the CV curves of the MoO_3/PANI/PPy electrode at various scan rates (Fig. S11, ESI†), the oxidation and reduction peaks ascribed to PANI are not that obvious compared to those of the

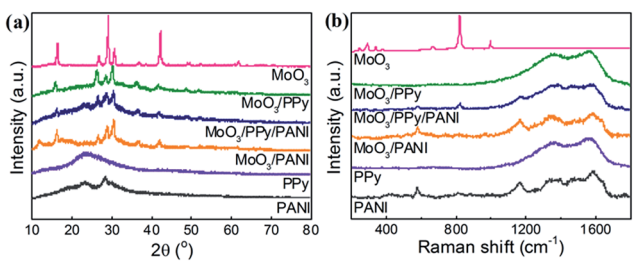

Fig. 4 (a) XRD patterns and (b) Raman spectra of MoO_3, MoO_3/PPy, MoO_3/PPy/PANI, MoO_3/PANI, PPy and PANI.

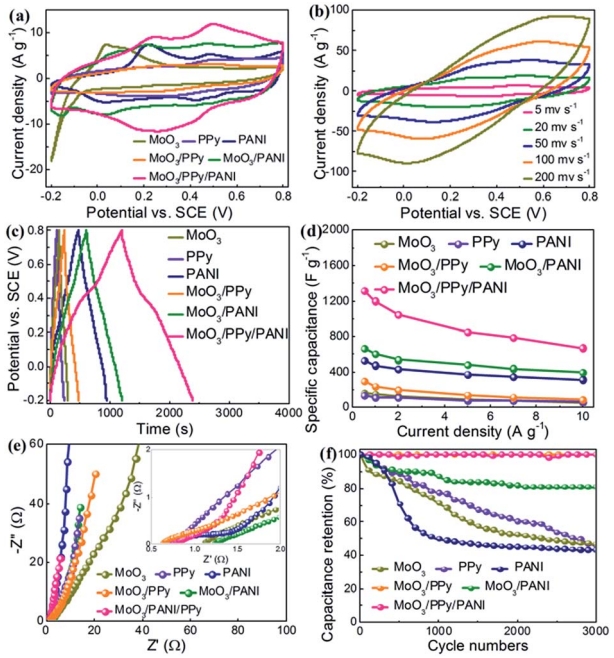

Fig. 5 (a) CV curves of the MoO_3, MoO_3/PPy, MoO_3/PPy/PANI, MoO_3/PANI, PPy and PANI electrodes at a scan rate of 10 mV s^{-1}. (b) CV curves of the MoO_3/PPy/PANI electrode at scan rates ranging from 5 to 200 mV s^{-1}. (c) Galvanostatic charge/discharge curves of the MoO_3, MoO_3/PPy, MoO_3/PPy/PANI, MoO_3/PANI, PPy and PANI electrodes at 1 A g^{-1}. (d) Specific capacitances of the MoO_3, MoO_3/PPy, MoO_3/PPy/PANI, MoO_3/PANI, PPy and PANI electrodes at current densities ranging from 0.5 to 10 A g^{-1}. (e) EIS curves of the MoO_3, PPy, PANI, MoO_3/PPy, MoO_3/PANI and MoO_3/PPy/PANI electrodes at open-circuit potentials. The inset of (e) shows the EIS curves of these electrodes in the high-frequency region. (f) Cycling stability of the MoO_3, MoO_3/PPy, MoO_3/PPy/PANI, MoO_3/PANI, PPy and PANI electrodes for 3000 charge/discharge cycles at a current density of 2 A g^{-1}.

MoO_3/PPy/PANI electrode, indicating that a lower capacitance contribution of PANI is achieved because the inner PANI within the MoO_3/PPy/PANI composites does not make good contact with the electrolytic ions. Therefore, the immobilization of PANI on the outer layer shows superiority in terms of the order of construction of the core–shell structure with respect to PPy and PANI in these ternary composites. The reversible redox reactions of the neat PANI electrode reveal oxidation peaks at 0.2 and 0.5 V and reduction peaks at 0.04 and 0.42 V, respectively. The peaks centered at 0.2 and 0.5 V are attributed to the redox transition of PANI from a semiconducting state to a conducting state and then to pernigraniline.[36] The MoO_3/PPy/PANI electrode shows similar redox peaks to those of PANI and MoO_3/PANI electrodes, but exhibits a larger CV surrounding area than those of its single components and binary composites at the same scan rate, indicating that the MoO_3/PPy/PANI electrode has larger specific capacitances than those of neat conducting polymers or MoO_3/conducting polymer binary composite electrodes. The excellent capacitance and rate capability of the MoO_3/PPy/PANI architectures are explained as follows: (i) the MoO_3/PPy core–shell structures within the ternary composites provide highly conductive paths for electron transport as well as a well-defined substrate for the decoration of PANI nanowire arrays, and (ii) the PANI nanowire arrays within the MoO_3/PPy/PANI composites exhibit enhanced electrode/electrolyte interfacial areas. Fig. 5b presents the CV curves of the MoO_3/PPy/PANI electrode at scan rates ranging from 5 to 200 mV s^{-1}. The shape of these CV curves with mirror-image features does not significantly change even at a high scan rate of 200 mV s^{-1}, demonstrating an ideal capacitive behavior with an excellent rate capability.

The galvanostatic charge/discharge curves at various current densities in the voltage window of −0.2–0.8 V were measured to further investigate the capacitance performances of these electrodes. The MoO_3/PPy/PANI electrode possesses the longest discharge time compared with other electrodes (Fig. 5c), indicating its higher specific capacitance among various electrodes. Besides, it is worth mentioning that the MoO_3/PPy shows a higher specific capacitance than neat MoO_3 and PPy, which can be ascribed to reduced internal resistances due to the surrounding PPy layers on the MoO_3.[37] From calculations of the discharge time from the galvanostatic charge/discharge curves, the relationships of the specific capacitances as a function of the current densities for all the samples were calculated and are shown in Fig. 5d. The specific capacitances of all the electrodes decrease with the increase of current density. The reason might be that at the high current density, the lack of contact between the electrode and the electrolyte contributes to incomplete redox reactions. The MoO_3/PPy/PANI electrode shows higher specific capacitance in comparison with other electrodes at various current densities, indicating that the combination of MoO_3 with these two conducting polymers might effectively enhance the specific capacitances by the synergistic effects of each component. A desirable specific capacitance of 1315 F g^{-1} is obtained for the MoO_3/PPy/PANI electrode at a current density of 0.5 A g^{-1}, compared to 159, 135, 527, 297 and 660 F g^{-1} for the MoO_3, PPy, PANI, MoO_3/PPy and MoO_3/PANI electrodes, respectively. Even at a high current density of 10 A g^{-1}, the specific capacitance of the MoO_3/PPy/PANI still remains at 672 F g^{-1}, while specific capacitances of only 316 and 394 F g^{-1} are obtained for neat PANI and MoO_3/PANI electrodes.

In order to calculate the theoretical value of the ternary composite electrode, the weight content of each component in the MoO_3/PPy/PANI composites needs to be quantified. Therefore, thermal gravimetric analysis (TGA) of the MoO_3, MoO_3/PANI, and MoO_3/PPy/PANI in air at a heating rate of 10 °C min^{-1} was conducted and the results are presented in Fig. S12 (ESI†). Neat MoO_3 remains stable over the entire temperature range below 600 °C. The MoO_3/PPy exhibits a weight loss of ~25 wt% between 50 and 600 °C, owing to the combustion of PPy. The PPy content in the MoO_3/PPy is determined to be ~25 wt%. For the MoO_3/PPy/PANI, the weight loss at 50–200 °C corresponds to the removal of the adsorbed water. The weight ratio of MoO_3/PPy/PANI could also be determined from the TGA curves taking into account that the residual weight at 600 °C refers to the MoO_3. Therefore, the content of MoO_3 within the MoO_3/PPy/PANI is ~12.5%, and the content of PPy and PANI is ~4.2 wt% and ~83.3 wt%, respectively. Theoretical and literature results indicate that the theoretical specific capacitances (C_s) of MoO_3, PPy and PANI are 2700, 620 and 750 F g^{-1}.[38–40] For the MoO_3/

PPy/PANI composites with the measured MoO_3 : PPy : PANI mass ratio, the theoretical specific capacitance of the composites is calculated to be 988.3 F g^{-1}. The practical specific capacitance of the MoO_3/PPy/PANI composites in this study is found to be 1315 F g^{-1} at a current density of 0.5 A g^{-1}, which is higher than the theoretical capacitances. The practical specific capacitance is a combination of electrical double-layer capacitances and pseudocapacitances while the theoretical capacity only takes the pseudocapacitances into consideration.[41] Besides, the MoO_3/PPy/PANI composites with the unique PANI nanowire arrays could greatly enhance the efficiency of ion diffusion. In addition, the specific capacitances of the MoO_3/PANI/PPy electrode at various current densities are shown in Fig. S13 (ESI†). The capacitance of the MoO_3/PANI/PPy electrode only reaches 780 F g^{-1} at a current of 0.5 A g^{-1} and remains at 351.5 F g^{-1} at 10 A g^{-1}, which are much smaller than those of the MoO_3/PPy/PANI electrode. The significantly enhanced capacitance of MoO_3/PPy/PANI might be attributed to improved conductive pathways which promoted the electron and proton transfer processes.[42] Furthermore, the inner part (MoO_3/PPy) in the ternary composites not only offers a much larger surface area to load a large amount of PANI effectively with a high electrochemical utilization of PANI, but also acts as a nanoscale framework to provide more insertion and extraction paths for ions. Electrochemical impedance spectroscopy (EIS, Fig. 5e) was performed and Nyquist plots were measured to analyze the capacitive properties of these electrodes. The slope segments in the low-frequency region represent the ion diffusion resistances of the electrodes.[17] The MoO_3/PPy/PANI and PANI exhibit larger slopes than the other samples, demonstrating that the MoO_3/PPy/PANI and PANI electrodes exhibit lower ion diffusion resistances due to the introduction of the highly porous structures. In the high-frequency region, the intercepts of the *x*-axis give the electron transfer resistances (R_s). The R_s of MoO_3, PANI, PPy, MoO_3/PPy, MoO_3/PANI and MoO_3/PPy/PANI are 1.12, 0.76, 0.73, 0.62, 1.23 and 0.73 Ω, respectively. The R_s value of the MoO_3 efficiently decreases when combined with PPy, revealing an excellent interfacial contact between the MoO_3 nanobelt and the immobilized PPy. However, when the PANI nanowires are grown on the surface of MoO_3, the R_s of MoO_3/PANI is not as low as that of MoO_3/PPy, indicating an inferior interfacial contact between the MoO_3 and the PANI nanowire arrays. Moreover, the MoO_3/PPy/PANI and MoO_3/PPy electrodes show smaller electron transfer resistances as compared to the other samples. The results indicate that the introduction of the PPy layer accelerates the electron transfer and therefore efficiently decreases the interfacial contact resistances of the composites.

Fig. 6a shows the CV curves of the MoO_3/PPy/PANI electrodes assembled in a two-electrode symmetric supercapacitor at scan rates of 0–1 V in a 0.5 M H_2SO_4 electrolyte. The CV curves exhibit distorted rectangular shapes indicating the contributions of both pseudocapacitances and electric double-layer capacitances. In addition, the shape of the CV curves remains undistorted at a high scan rate of 200 mV s^{-1}, indicating the low contact resistance and excellent rate capability in the device.[43] Fig. 6b presents the galvanostatic charge/discharge curves at various current densities between 0 and 1 V, and the specific

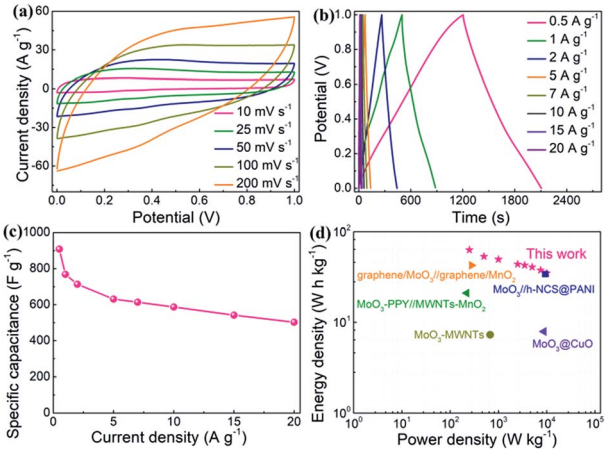

Fig. 6 (a) CV curves of the MoO_3/PPy/PANI//MoO_3/PPy/PANI symmetric supercapacitor at different scan rates. (b) Galvanostatic charge/discharge curves of the MoO_3/PPy/PANI//MoO_3/PPy/PANI symmetric supercapacitor at various current densities. (c) Specific capacitance of the MoO_3/PPy/PANI at various current densities. (d) Ragone plots of the assembled symmetric supercapacitor of MoO_3/PPy/PANI in comparison to other electrodes from the literature.

capacitances of the MoO_3/PPy/PANI electrode as a function of current densities are showed in Fig. 6c. At a current density of 0.5 A g^{-1}, the specific capacitance of the MoO_3/PPy/PANI electrode reaches 908.1 F g^{-1}; moreover, the MoO_3/PPy/PANI electrode displays an excellent rate performance and still delivers a large specific capacitance of 502.4 F g^{-1} at a high current density of 20 A g^{-1}. The Ragone plots of the two-electrode supercapacitor cell were calculated and are presented in Fig. 6d. The supercapacitor using the symmetric MoO_3/PPy/PANI electrodes exhibits an energy density of 63 W h kg^{-1} at a power density of 250 W kg^{-1}. The energy density of our supercapacitors is higher than those of the reported supercapacitors assembled from electrodes of MoO_3@CuO (7.9 W h kg^{-1} at 8726 W kg^{-1}),[44] MoO_3-PPy//MWNTs-MnO_2 (21.03 W h kg^{-1} at 220 W kg^{-1}),[45] MoO_3-MWNTs (7.28 W h kg^{-1} at 672 W kg^{-1}),[46] MoO_3//h-NCS@PANI (34.1 W h kg^{-1} at 9350.6 W kg^{-1}),[47] and graphene/MoO_3//graphene/MnO_2 (42.6 W h kg^{-1} at 276 W kg^{-1}).[48] Moreover, our supercapacitor retains 55% of its energy density with an incredible rate capability as the power density increases from 250 to 10 000 W kg^{-1}, indicating that these biomimetic *Setaria viridis*-inspired MoO_3/PPy/PANI composites are quite promising electrode materials for supercapacitors.

For practical applications, the self-discharge behavior of the supercapacitor device with a two-electrode configuration of symmetric MoO_3/PPy/PANI electrodes was evaluated by precharging the device to 1 V and then conducting an open-circuit potential test within 24 h (Fig. S14, ESI†). The supercapacitor device undergoes a rapid self-discharge process in the first few hours and then stabilizes at a constant voltage value of 0.68 V after 4 h. Therefore, the device has a desirable voltage retention rate with good prospects for practical development.[49] Cycling stability is critical to evaluating the performance of electrode materials for supercapacitors in

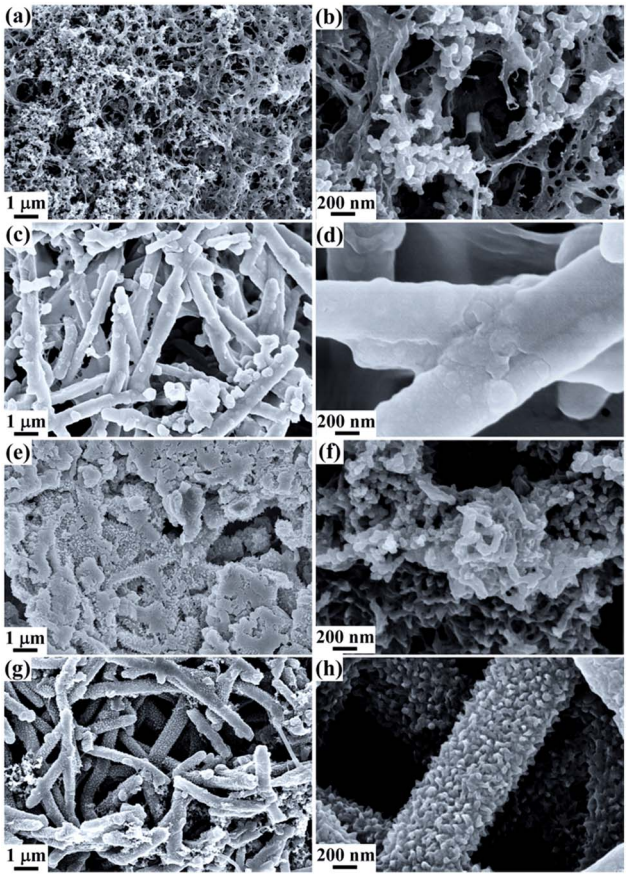

Fig. 7 SEM images of the (a and b) MoO_3, (c and d) MoO_3/PPy, (e and f) MoO_3/PANI and (g and h) MoO_3/PANI/PPy electrodes after 3000 charge/discharge cycles.

practical applications. The cycling stabilities of the MoO_3/PPy/PANI electrodes and other electrodes are investigated using repeated galvanostatic charge/discharge measurements at a current density of 2 A g^{-1} for 3000 cycles (Fig. 5f). The corresponding galvanostatic charge/discharge curves of the MoO_3, PANI, PPy, MoO_3/PANI, MoO_3/PPy, MoO_3/PPy/PANI electrodes for 3000 charge/discharge cycles at a current density of 2 A g^{-1} are provided in Fig. S15† (ESI). A synergetic effect of MoO_3 and individual conducting polymers in the binary composites is demonstrated from the capacitance retention of MoO_3/PPy (100%) and MoO_3/PANI (80.6%), compared with the neat PPy (46%), PANI (43.1%) and MoO_3 (46.5%) electrodes after 3000 charge/discharge cycles. More importantly, the rationally combined MoO_3/PPy/PANI ternary composites can achieve a significant enhancement of cycling stability with an almost 100% retention compared with that of the MoO_3/PANI (80.6%), indicating the necessity for the immobilization of ultrathin PPy layers on the MoO_3 nanobelts. Besides, the life span of the MoO_3/PPy/PANI was investigated with more cycles at a relatively large current density, and the cycling stability of the MoO_3/PPy/PANI electrode after 20 000 charge/discharge cycles at 10 A g^{-1} as well as the corresponding galvanostatic charge/discharge curves for 101–110 and 19 991–20 000 charge/discharge cycles were measured and the results are shown in Fig. S16 (ESI†). After 20 000 charge/discharge cycles at 10 A g^{-1}, the MoO_3/PPy/PANI electrode still exhibits a superior capacitance retention of 86%. Additionally, the SEM images of MoO_3, MoO_3/PANI, MoO_3/PPy and MoO_3/PPy/PANI after the cycling tests were recorded to illustrate the mechanisms for the largely enhanced cycling stability of the ternary composites. For neat MoO_3 after cycling (Fig. 7a and b), severely damaged MoO_3 is observed. The drastic capacitance degradation of the MoO_3 could be explained by its structural instability for the intercalation of H^+ ions into the interlayers of MoO_3. When the PPy layer was coated onto the MoO_3, no obvious structural changes in the MoO_3/PPy were observed (Fig. 7c and d), indicating the efficient protection of the MoO_3 core from dissolution and collapse due to the PPy coating layers. Without the PPy coating, after cycling, the MoO_3/

Table 1 Supercapacitive performance comparison of the biomimetic *Setaria viridis*-inspired MoO_3/PPy/PANI with other PANI or PPy-based composites in the literature

Electrode materials	Electrolyte	Specific capacitance (F g^{-1})	Rate performance (F g^{-1})	Cycling stability	Ref.
Flower-like PANI/graphene	1 M H_2SO_4	1510 at 1A g^{-1}	851 at 15 A g^{-1}	89% (1500 cycles)	50
PANI nanotubes/rGO	0.2 M phosphate	1967 at 1A g^{-1}	639 at 10 A g^{-1}	89.7% (5000 cycles)	51
Hollow graphene/PANI nanospheres	1 M H_2SO_4	554 at 0.5 A g^{-1}	463 at 10 A g^{-1}	80% (2000 cycles)	52
1T-MoS_2/PANI nanosheets	0.5 M H_2SO_4	470 at 0.5 A g^{-1}	340 at 10 A g^{-1}	91% (2000 cycles)	53
Core–shell PPy/PANI nanotubes	1 M H_2SO_4	419 at 5 mA cm^{-2}	375 at 15 mA cm^{-2}	None	54
MoO_3/PANI nanobelts	1 M H_2SO_4	632 at 1 A g^{-1}	379 at 10 A g^{-1}	76.7% (3000 cycles)	55
Tubular MoS_2/PANI	1 M H_2SO_4	552 at 0.5 A g^{-1}	455 at 30 A g^{-1}	88% (1000 cycles)	37
MoS_2/PPy	1 M KCl	695 at 0.5 A g^{-1}	500 at 10 A g^{-1}	85% (4000 cycles)	32
Honeycomb-like Fe_2O_3 nanoflake/PPy arrays	0.5 M Na_2SO_4	1168 at 1 A g^{-1}	113 at 10 A g^{-1}	97.1% (3000 cycles)	46
Tubular MoS_2/PPy	0.5 M Na_2SO_4	462 at 1 A g^{-1}	261 at 10 A g^{-1}	82% (3000 cycles)	26
Graphene oxide/PPy/MWNTs	1 M $NaNO_3$	407 at 1 A g^{-1}	245.2 at 3 A g^{-1}	92% (1000 cycles)	56
Branchlike MoO_3/PPy	1 M Na_2SO_4	123 at 0.27 A g^{-1}	104 at 2.67 A g^{-1}	90% (200 cycles)	57
PANI/C nanowire	1 M H_2SO_4	189.73 at 0.5 mA cm^{-2}	158 at 10 mA cm^{-2}	95% (10 000 cycles)	58
PANI nanofiber	1 M H_2SO_4	636 at 2 A g^{-1}	626 at 25 A g^{-1}	83% (10 000 cycles)	59
PANI/RGO aerogel	1 M H_2SO_4	480 at 1 A g^{-1}	334 at 40 A g^{-1}	96.1% (10 000 cycles)	60
Yolk–shell Ni–CeO_2/PANI nanospheres	1 M Na_2SO_4	866 at 1 A g^{-1}	280 at 20 A g^{-1}	85.6% (10 000 cycles)	61
***Setaria viridis*-inspired MoO_3/PPy/PANI**	**0.5 M H_2SO_4**	**1315 at 0.5 A g^{-1}**	**672 at 10 A g^{-1}**	**86% (20 000 cycles)**	**This work**

PANI shows a slight aggregation of PANI nanowires to the extent that the 1D outline of MoO_3 is maintained well (Fig. 7e and f). The maintenance of the nanobelt structure of the MoO_3 might improve the cycling stability of the MoO_3/PPy/PANI electrode (Fig. 7g and h). More importantly, the nanowire arrays of the MoO_3/PPy/PANI composites are roughly maintained after cycling, and no obvious changes are observed, revealing the good interfacial contact between the intermediate PPy, the inner MoO_3 and the outermost PANI. Moreover, compared with previously reported PANI or PPy-based composite electrodes for supercapacitors (Table 1), our biomimetic *Setaria viridis*-inspired MoO_3/PPy/PANI electrodes show competitive capacitances and rate capacitances. It should be specially noted that the extremely high cycling stability of the MoO_3/PPy/PANI electrodes verifies the design of the *Setaria viridis*-inspired nanostructures as a promising electrode material with both high specific capacitance and good cycling stability. The excellent performance of the MoO_3/PPy/PANI electrodes is attributed to the following reasons: (i) the presence of the MoO_3 nanobelt core acting as a unique template to load conducting polymers with a high surface area with more ion-accessible sites; (ii) the ultrathin PPy layers acting as a buffer layer between MoO_3 and PANI could effectively overcome the aggregation of PANI during cycling and provide shortened pathways for insertion and extraction of ions; and (iii) the MoO_3 nanobelt core itself and the pores of the PANI nanowire array structure could provide large ion reservoirs especially for fast insertion and extraction of ions. Therefore, the above-mentioned optimized nanostructures and synergistic effects between the MoO_3 nanobelts, ultrathin PPy layers and PANI nanowires effectively endow the resultant MoO_3/PPy/PANI ternary composites with high specific capacitance, excellent rate capability and excellent long-term cycling stability.

Conclusion

In summary, we have developed a facile strategy to fabricate MoO_3/PPy/PANI ternary composites by mimicking the *Setaria viridis* structure, which could efficiently enhance the electrode performance due to largely improved structural stability and fast transport of ions and electrons between the electrodes. As a result, the MoO_3/PPy/PANI ternary composites deliver much higher specific capacitance (1315 F g^{-1} at 0.5 A g^{-1}) than their individual components and binary composites. The MoO_3/PPy/PANI ternary composites also exhibit an excellent rate capability of 672 F g^{-1} at 10 A g^{-1}, a high energy density of 63 W h kg^{-1}, and an extremely long cycle life with a capacitance retention of 86% up to 20 000 cycles. The present nanoengineering strategy can be further extended to prepare various biomimetic nanomaterials for advanced electrode materials through scalable and low-cost routes.

Conflicts of interest

There are no conflicts to declare.

Acknowledgements

We are grateful for the financial support from the National Natural Science Foundation of China (51433001, 21504012 and 51773035), the Fundamental Research Funds for the Central Universities (17D110606), the Program of Shanghai Subject Chief Scientist (17XD1400100), the Natural Science Foundation of Shanghai (17ZR1439900), the Shanghai Rising-Star Program (18QA1400200) and the Shanghai Scientific and Technological Innovation Project (18JC1410600).

References

1 J. Yang, Y. Liu, S. Liu, L. Li, C. Zhang and T. Liu, *Mater. Chem. Front.*, 2017, **1**, 251–268.
2 L. L. Zhang and X. S. Zhao, *Chem. Soc. Rev.*, 2009, **38**, 2520–2531.
3 Z. N. Yu, L. Tetard, L. Zhai and J. Thomas, *Energy Environ. Sci.*, 2015, **8**, 702–730.
4 W. Wei, X. Cui, W. Chen and D. G. Ivey, *Chem. Soc. Rev.*, 2011, **40**, 1697–1721.
5 S. Padmajan Sasikala, K. E. Lee, J. Lim, H. J. Lee, S. H. Koo, I. H. Kim, H. J. Jung and S. O. Kim, *ACS Nano*, 2017, **11**, 9424–9434.
6 M. Tebyetekerwa, S. Yang, S. Peng, Z. Xu, W. Shao, D. Pan, S. Ramakrishna and M. Zhu, *Electrochim. Acta*, 2017, **247**, 400–409.
7 B. Li, F. Dai, Q. Xiao, L. Yang, J. Shen, C. Zhang and M. Cai, *Energy Environ. Sci.*, 2015, **9**, 102–106.
8 G.-F. Chen, X.-X. Li, L.-Y. Zhang, N. Li, T. Y. Ma and Z.-Q. Liu, *Adv. Mater.*, 2016, **28**, 7680–7687.
9 M. Tebyetekerwa, Z. Xu, W. Li, X. Wang, I. Marriam, S. Peng, S. Ramkrishna, S. Yang and M. Zhu, *ACS Appl. Energy Mater.*, 2018, **1**, 377–386.
10 J. Liu, J. Jiang, C. Cheng, H. Li, J. Zhang, H. Gong and H. J. Fan, *Adv. Mater.*, 2011, **23**, 2076–2081.
11 T. Zhai, L. Wan, S. Sun, Q. Chen, J. Sun, Q. Xia and H. Xia, *Adv. Mater.*, 2017, **29**, 1604167.
12 L. Huang, B. Yao, J. Sun, X. Gao, J. Wu, J. Wan, T. Li, Z. Hu and J. Zhou, *J. Mater. Chem. A*, 2017, **5**, 2897–2903.
13 L. Zhu, C. K. N. Peh, T. Zhu, Y.-F. Lim and G. W. Ho, *J. Mater. Chem. A*, 2017, **5**, 8343–8351.
14 Q. Meng, K. Cai, Y. Chen and L. Chen, *Nano Energy*, 2017, **36**, 268–285.
15 G. Zhang, X. Xiao, B. Li, P. Gu, H. Xue and H. Pang, *J. Mater. Chem. A*, 2017, **5**, 8155–8186.
16 M.-S. Balogun, Y. Huang, W. Qiu, H. Yang, H. Ji and Y. Tong, *Mater. Today*, 2017, **20**, 425–451.
17 M. Tebyetekerwa, X. Wang, Y. Wu, S. Yang, M. Zhu and S. Ramakrishna, *J. Mater. Chem. A*, 2017, **5**, 21114–21121.
18 Z. Huang, L. Li, Y. Wang, C. Zhang and T. Liu, *Compos. Commun.*, 2018, **8**, 83–91.
19 W. He, C. Wang, F. Zhuge, X. Deng, X. Xu and T. Zhai, *Nano Energy*, 2017, **35**, 242–250.
20 H. Tang, J. Wang, H. Yin, H. Zhao, D. Wang and Z. Tang, *Adv. Mater.*, 2015, **27**, 1117–1123.

21 R. B. Ambade, S. B. Ambade, N. K. Shrestha, R. R. Salunkhe, W. Lee, S. S. Bagde, J. H. Kim, F. J. Stadler, Y. Yamauchi and S.-H. Lee, *J. Mater. Chem. A*, 2017, **5**, 172–180.
22 J. Peng and Q. Cheng, *Adv. Mater.*, 2017, **29**, 1702959.
23 Y. Liu, G. Li, Z. Chen and X. Peng, *J. Mater. Chem. A*, 2017, **5**, 9775–9784.
24 P. Ma, Z. Zhou, J. Dai, L. Qin, X. Ye, X. Chen, J. He, A. Xie, Y. Yan and C. Li, *RSC Adv.*, 2016, **6**, 9619–9630.
25 Y. Liu, B. Zhang, Y. Yang, Z. Chang, Z. Wen and Y. Wu, *J. Mater. Chem. A*, 2013, **1**, 13582–13587.
26 Y. Chen, W. Ma, K. Cai, X. Yang and C. Huang, *Electrochim. Acta*, 2017, **246**, 615–624.
27 H. S. Kim, J. B. Cook, H. Lin, J. S. Ko, S. H. Tolbert, V. Ozolins and B. Dunn, *Nat. Mater.*, 2017, **16**, 454–460.
28 X. Yang, H. Ding, D. Zhang, X. Yan, C. Lu, J. Qin, R. Zhang, H. Tang and H. Song, *Cryst. Res. Technol.*, 2011, **46**, 1195–1201.
29 D. Liu, W. Lei, J. Hao, D. Liu, B. Liu, X. Wang, X. Chen, Q. Cui, G. Zou and J. Liu, *J. Appl. Phys.*, 2009, **105**, 023513.
30 X. Sui, Y. Chu, S. Xing and C. Liu, *Mater. Lett.*, 2004, **58**, 1255–1259.
31 Z. Zhang, Z. Wei and M. Wan, *Macromolecules*, 2002, **35**, 5937–5942.
32 H. Tang, J. Wang, H. Yin, H. Zhao, D. Wang and Z. Tang, *Adv. Mater.*, 2015, **27**, 1117–1123.
33 L. Q. Mai, B. Hu, W. Chen, Y. Qi, C. Lao, R. Yang, Y. Dai and Z. L. Wang, *Adv. Mater.*, 2007, **19**, 3712–3716.
34 Z. Liu, B. Ye, M. Jin, H. Chen, H. Zhong, X. Wang and Z. Guo, *Nanoscale*, 2015, **7**, 6754–6761.
35 G. M. do Nascimento, C. H. Silva and M. L. Temperini, *Macromol. Rapid Commun.*, 2006, **27**, 255–259.
36 G. Xu, N. Wang, J. Wei, L. Lv, J. Zhang, Z. Chen and Q. Xu, *Ind. Eng. Chem. Res.*, 2012, **51**, 14390–14398.
37 L. Ren, G. Zhang, Z. Yan, L. Kang, H. Xu, F. Shi, Z. Lei and Z.-H. Liu, *ACS Appl. Mater. Interfaces*, 2015, **7**, 28294–28302.
38 G. A. Snook, P. Kao and A. S. Best, *J. Power Sources*, 2011, **196**, 1–12.
39 V. Kumar and P. S. Lee, *J. Phys. Chem. C*, 2015, **119**, 9041–9049.
40 W. Sugimoto, T. Ohnuma, Y. Murakami and Y. Takasu, *Electrochem. Solid-State Lett.*, 2001, **4**, A145–A147.
41 H. Li, J. Wang, Q. Chu, Z. Wang, F. Zhang and S. Wang, *J. Power Sources*, 2009, **190**, 578–586.
42 H. Li, L. Xu, H. Sitinamaluwa, K. Wasalathilake and C. Yan, *Compos. Commun.*, 2016, **1**, 48–53.
43 N. Jabeen, A. Hussain, Q. Xia, S. Sun, J. Zhu and H. Xia, *Adv. Mater.*, 2017, **29**, 1700804.
44 Y. Zhang, B. Lin, J. Wang, P. Han, T. Xu, Y. Sun, X. Zhang and H. Yang, *Electrochim. Acta*, 2016, **191**, 795–804.
45 P. Du, W. Wei, D. Liu, H. Kang, C. Liu and P. Liu, *J. Mater. Sci.*, 2018, **53**, 5255–5269.
46 P.-Y. Tang, L.-J. Han, A. Genç, Y.-M. He, X. Zhang, L. Zhang, J. R. Galán-Mascarós, J. R. Morante and J. Arbiol, *Nano Energy*, 2016, **22**, 189–201.
47 X. Li, X. Xiang, Y. Liu and D. Xiao, *Appl. Surf. Sci.*, 2018, **442**, 476–486.
48 X. Fan, C. Yu, Z. Ling, J. Yang and J. Qiu, *ACS Appl. Mater. Interfaces*, 2013, **5**, 2104–2110.
49 Z. Fan, J. Yan, L. Zhi, Q. Zhang, T. Wei, J. Feng, M. Zhang, W. Qian and F. Wei, *Adv. Mater.*, 2010, **22**, 3723–3728.
50 F. Ke, Y. Liu, H. Xu, Y. Ma, S. Guang, F. Zhang, N. Lin, M. Ye, Y. Lin and X. Liu, *Compos. Sci. Technol.*, 2017, **142**, 286–293.
51 M. F. Mousavi, M. Hashemi, M. S. Rahmanifar and A. Noori, *Electrochim. Acta*, 2017, **228**, 290–298.
52 J. Luo, Y. X. Chen, Y. Zheng, C. B. B. Wang, W. Wei and X. Y. Liu, *Electrochim. Acta*, 2018, **272**, 221–232.
53 C. Zhao, J. M. Ang, Z. Liu and X. Lu, *Chem. Eng. J.*, 2017, **330**, 462–469.
54 H. Mi, X. Zhang, X. Ye and S. Yang, *J. Power Sources*, 2008, **176**, 403–409.
55 B. You, J. Jiang and S. Fan, *ACS Appl. Mater. Interfaces*, 2014, **6**, 15302–15308.
56 B. Wang, J. Qiu, H. Feng and E. Sakai, *Electrochim. Acta*, 2015, **151**, 230–239.
57 X. Zhang, X. Zeng, M. Yang and Y. Qi, *ACS Appl. Mater. Interfaces*, 2014, **6**, 1125–1130.
58 T. Liu, L. Finn, M. Yu, H. Wang, T. Zhai, X. Lu, Y. Tong and Y. Li, *Nano Lett.*, 2014, **14**, 2522–2527.
59 K. Zhou, Y. He, Q. Xu, Q. Zhang, A. Zhou, Z. Lu, L. K. Yang, Y. Jiang, D. Ge, X. Y. Liu and H. Bai, *ACS Nano*, 2018, DOI: 10.1021/acsnano.8b02055.
60 Z. Gao, J. Yang, J. Huang, C. Xiong and Q. Yang, *Nanoscale*, 2017, **9**, 17710–17716.
61 Q. Gong, Y. Li, H. Huang, J. Zhang, T. Gao and G. Zhou, *Chem. Eng. J.*, 2018, **344**, 290–298.

